iScience

CellPress
OPEN ACCESS

Article

De-risking fault leakage risk and containment integrity for subsurface storage applications

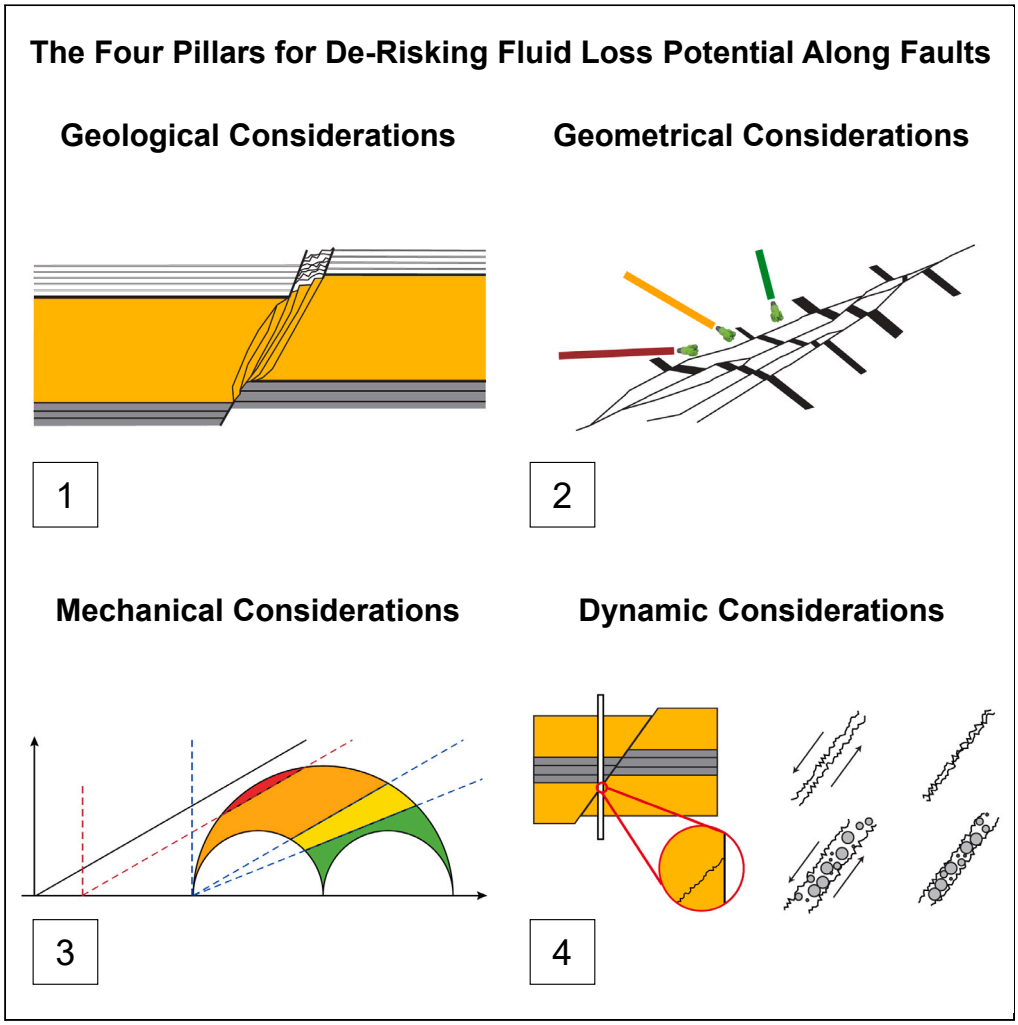

Kevin Bisdom,
Alvin W. Chan

kevin.bisdom@shell.com

Highlights

A novel probabilistic Coulomb Failure Stress workflow to assess fault integrity

Workflow supports early risk ranking of subsurface energy and CO_2 storage sites

Applied to the Decatur CO_2 storage project to rank faults based on containment risk

Faults with large throw to reservoir thickness ratio show higher reactivation risk

Bisdom & Chan, iScience *27*, 109957
June 21, 2024 © 2024 The Author(s). Published by Elsevier Inc.
https://doi.org/10.1016/j.isci.2024.109957

iScience

CellPress
OPEN ACCESS

Article

De-risking fault leakage risk and containment integrity for subsurface storage applications

Kevin Bisdom[1,3,*] and Alvin W. Chan[2]

SUMMARY

The subsurface is pivotal in the energy transition, for the sequestration of CO_2 and energy storage. It is crucial to understand to what extent geological faults may form leakage pathways that threaten the containment integrity of these projects. Fault flow behavior has been studied in the context of hydrocarbon development, supported by observations from wells drilled through faults, but such observations are rare in geoenergy projects. Focusing on mechanical behavior as early indicator of potential leakage risks, a probabilistic Coulomb Failure Stress workflow is developed and demonstrated using data from the Decatur CO_2 sequestration project to rank faults based on their containment risk. The analysis emphasizes the importance of fault throw relative to reservoir thickness and pore pressure change in assessing reactivation risks. Integrating this mechanical assessment with geological and dynamic fault analyses contributes to derisking fault containment for geoenergy applications, providing valuable insights for the successful development of subsurface storage projects.

INTRODUCTION

Within the next decades, the use of the deep subsurface for geoenergy applications is likely to increase as the number of storage projects for CO_2 and subsurface energy storage (e.g., hydrogen) and extraction (e.g., methane, geothermal) is expected to grow. Carbon Capture and Sequestration (CCS) alone needs to scale up from storing millions of tons of CO_2 per year at present to a scale of gigaton storage per year.[1] For gigaton storage to have a significant impact on reducing the concentration of CO_2 in the atmosphere, there cannot be any significant leakage of CO_2 out of the storage complex.[2] Current operating commercial-scale projects have demonstrated that the sequestration of CO_2 in the deep subsurface provides a safe long-term storage solution.[3–8] These existing projects do have the advantage of access to privileged pore space, with limited or no legacy wells or faults within the storage license area that could threaten containment integrity. Upscaling CCS from the current megaton scale to the yearly injection of gigatons will require making use of pore space with faults within the storage area, as geological faults are ubiquitous in the subsurface and injection near faults cannot always be avoided. Faults similarly form a potential threat to storage integrity for subsurface hydrogen storage[9] or cold water breakthrough in geothermal projects. As long as injection near faults does not induce leakage or induced seismicity, successful storage projects could include faults, but given the wide array of possible fault geometries and compositions, identification of faults that pose a potential containment threat is not straightforward.

Faults intersecting the primary seal of a storage site could under certain conditions be conductive, acting as a conduit for CO_2 or other stored fluids to migrate out of the storage site into the overburden (Figure 1). The risk for fault-related leakage needs to be quantified as part of the storage site permit application and in instances where the potential for fault leakage cannot be sufficiently de-risked, injection near susceptible faults needs to be avoided. Leakage of reservoir fluids into the overburden through conductive faults has been observed in the hydrocarbon industry,[10,11] as well as for natural occurrences of CO_2 in the subsurface.[12–15]

The probability of a fault acting as a conduit or barrier depends on the fault geometry, including the fault damage zone size and composition, the maximum burial depth and corresponding temperature and pressure history and the stress states over geological time and present-day storage conditions.[16,17] The lateral flow potential across a fault plane has been studied extensively in the context of reservoir compartmentalization resulting in transmissibility definitions based on concepts such as the Shale-Gouge-Ratio (SGR), often calibrated using transient pressure data from wells on both sides of the fault.[18–21] The SGR model focuses only on the fault core as the core is assumed to have the lowest permeability, forming the limiting factor of cross-fault flow. Containment integrity for subsurface storage activities requires however an assessment of the vertical, along-fault integrity risk, i.e., in the up-dip direction parallel to the main fault plane (red flow paths in Figure 1). The flow potential in this direction is defined by the sum of flow contributions from all fault zone components, not just the core.[22,23]

Assessing fault-related containment risks in the subsurface requires an integrated approach of along- and across-fault leakage through the characterization of the geological, mechanical and fluid flow characteristics of fault zones.[12,24–33] However, dedicated workflows for CCS and hydrogen storage that integrate all these components remain rare. Figure 2 shows the four main components that control fluid flow along

[1]Shell Global Solutions International B.V., The Hague, the Netherlands
[2]Shell Global Solutions U.K., Aberdeen, UK
[3]Lead contact
*Correspondence: kevin.bisdom@shell.com
https://doi.org/10.1016/j.isci.2024.109957

This is an open access article under the CC BY-NC-ND license (http://creativecommons.org/licenses/by-nc-nd/4.0/).

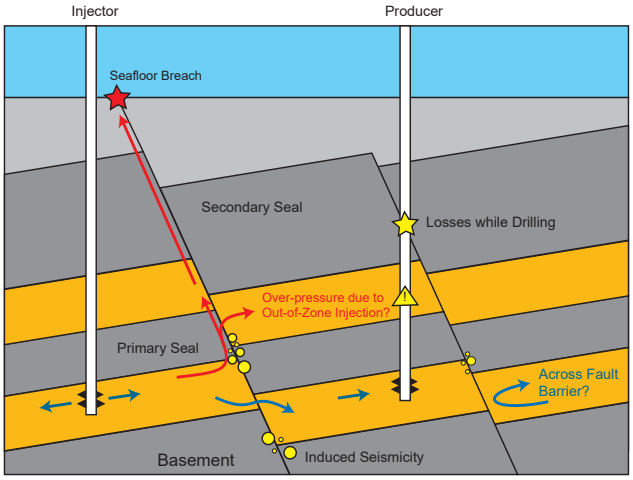

Figure 1. Sketch illustrating the possible flow paths that influence potential consequences of impaired fault integrity

The blue arrows indicate how the injected fluids can migrate laterally through the storage reservoir and adjacent fault blocks. The red arrows show possible vertical flow paths along the fault surfaces into overlying aquifers or to the seabed. The yellow and red features represent potential hazards associated with injection, including leakage to the seafloor, induced seismicity, out of zone injection and losses (during drilling).

faults introduced by Chan et al.[34] While designed for drilling through faults, this integrated analysis can be replicated with minor modifications to faults in the context of containment integrity for CO_2 storage and other fluid injection sites in proximity to subsurface faults (e.g., geothermal energy and hydrogen storage). In this article, we will demonstrate how we adapt and apply this workflow developed for safe drilling operations into a framework to rank fault integrity risks for CO_2 storage sites. The focus will be on the mechanical integrity of faults as reactivation-induced seismic activity and stress-induced fault leakage are key potential threats to the storage integrity of subsurface energy storage projects. The resulting fault integrity ranking framework helps identify faults that could pose a threat to containment integrity. While it provides no explicit quantification of leakage or seismicity risks, the ranking is based on a probabilistic framework to capture the large uncertainty space that is typically associated with subsurface geoenergy applications. The workflow is demonstrated using a case study of injection-induced fault reactivation in the Decatur CCS project in Illinois, USA.[35]

The four pillars for fault integrity

Faults are ubiquitous in the subsurface and they pose various levels of threats to geoenergy applications ranging from exploration and development of hydrocarbons and geothermal resources, well abandonment, CO_2 storage and hydrogen storage. For instance, a fault that poses no threat to drilling a well could be a major top seal leakage risk for long term injection and storage projects. To thoroughly investigate the

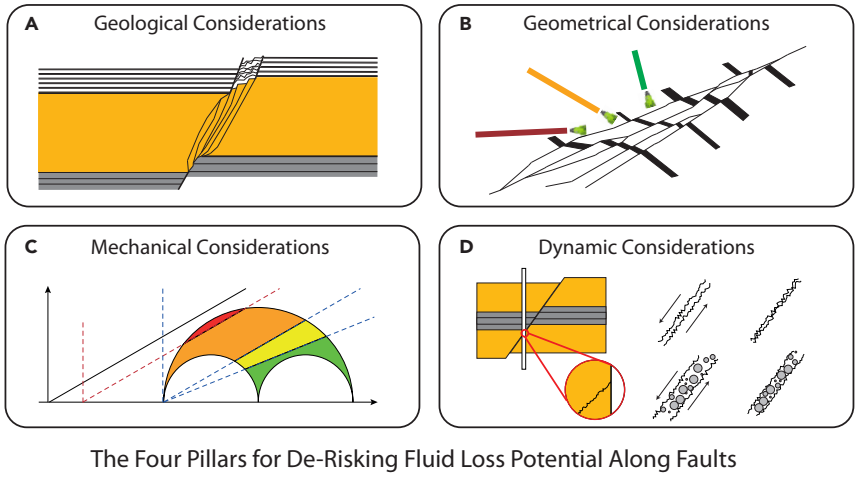

Figure 2. The four pillars for fault integrity

(A) Geological considerations, such as the fault type or damage zone dimensions; (B) Geometrical, referring to the fault in relation to wells drilled through the fault or injector wells in the vicinity; (C) Mechanical, addressing the mechanical reactivation potential of faults and (D) Dynamic, focusing on the flow behavior of the fault zone.

potential impacts of drilling through faults, a systematic integrated assessment framework was introduced by Chan et al.[34] The framework was set up with well engineering in mind and takes into consideration fault characterizations from various aspects: Geological, geometrical, mechanical and dynamic behavior (Figure 2). Dynamic refers to the fluid flow behavior within the fault zone. While the original design of the framework focused on well design and drilling strategy, the same concept can be applied for evaluating fault integrity during fluid injection with some minor modifications to the various pillars:

- Geological considerations – the first pillar represents the static architecture of the risk assessment framework and is driven by geological and geophysical evaluations. The focus is to assess the presence and the complexity of the fault zone. For example, assessing the confidence level of the existence of an interpreted fault, the impact of basin or structural evolution on the fault zone architecture and the impact of lithology on fault zone complexity.
- Geometrical considerations – In the context of well engineering this pillar focuses on the geometry between the well and the fault zone, since the area of exposure in a wellbore may lead to operational challenges. This pillar is one of the easiest to be modified in the design phase of a subsurface development project. However, geometrical considerations can be further extended to estimate the size of the damage zone from observed fault throw or offset, to guide placement of injection points to minimize leakage and seismicity risks for e.g., CO_2 sequestration. In other words, how close should and injection point be to minimize potential leakage threats posed by a fault damage zone?
- Mechanical considerations – The threshold at which mechanical failure can occur along a fault zone. Stress changes induced by for example CO_2 injection or seasonal storage of hydrogen can result in normal and shear stress changes along faults, potentially inducing microseismic events or stress-dependent changes in fault permeability. This pillar is the main subject of investigation of this article and will be discussed in greater details in the following sections.
- Dynamic considerations – One commonly missed element when evaluating fluid loss or leakage potential along a fault damage zone is the fluid flow behavior within the fault damage zone. The dynamic flow behavior can be affected by various factors from operational constraints (i.e., flow rate), fluid rheology, pressure-induced stress changes to stress-dependent fault and fracture permeability. This pillar can be the most complex among the four pillars yet provides opportunities for engineering design to mitigate some of the challenges. Chan et al.[36] have demonstrated that lost circulation materials (LCM), when deployed properly, can effectively cure losses across faulted (or fractured) zone and strengthen the pressure threshold such that subsequent drilling and completion activities can be conducted with a downhole fluid pressure exceeding the mechanical failure limits. Meanwhile, stress-dependent along-fault permeability changes during the production/injection period can also affect the threat profile of a "stable" or "sealing" fault. In case of a fault intersected by a well, the dynamic behavior can be measured directly; but in long-term CO_2 sequestration projects fault-well intersections are typically avoided, and there is typically no other direct measure of fault flow. In these projects, stress changes within the reservoir close to faults can serve as an indirect constraint on assessing potential changes in fault flow behavior.

Through an integrated assessment of these Four Pillars, threats of fluid losses and leakage potential across fault damage zone during the entire lifetime of the injection project (from well drilling to injection to post-injection monitoring) can be systematically risk-assessed. This integrated approach can improve the decision quality of well placement and design, drilling and completion fluid strategies, lost circulation management, injection philosophy and site monitoring and surveillance plans.

Mechanical integrity workflow

We extend the mechanical pillar from the Four Pillars workflow to include the effects of changes in pore pressure and fault offset on mechanical fault stability. In the absence of direct measurements of fault permeability, which are typically not available in CO_2 storage sites as drilling through faults is avoided,[37] we focus on mechanical integrity as a proxy for leakage risks. The along-fault permeability is partly influenced by the fault stress state, based on observations from the single-fracture scale[38] to subseismic fault damage zones[39–42] and seismic-scale faults.[32] Following the geological and geometric description of a fault, quantifying the change in fault stress associated with a pore pressure increase (storage or heating) or decrease (depletion or cooling) is the next step toward assessing fault integrity and aids in the relative ranking of fault-related containment risks between different faults in a potential storage site or across different prospective faulted store locations (Figure 3). A fault stress assessment can also contribute toward an improved understanding of induced seismicity risks, although a stress assessment in itself is insufficient to quantify these risks.

The risk of mechanical fault reactivation during injection is quantified by the change in Coulomb Failure Stress (CFS), based on the incremental normal and shear stress changes on a fault induced by pore pressure changes:

$$\Delta \mathrm{CFS} = \Delta\|\tau\| - \mu\left(\Delta\sigma_n - \Delta p_f\right) \qquad \text{(Equation 1)}$$

where τ and σ_n are the shear and normal stresses respectively, p_f the fluid pressure in the fault and μ is the static friction coefficient.[43] An increase in the CFS indicates a destabilizing effect on the mechanical fault integrity. The fault friction coefficient is typically the most challenging parameter to constrain, as *in-situ* measurements are rare and lab measurements are not easily upscaled.[44] Many studies assume a constant value of 0.6, but values as low as 0.4 have been observed based on field observations during a drilling campaign through a heavily faulted formation.[45]

To evaluate the CFS along an entire fault plane, Finite Element (FE) numerical models are often used.[29,35,46,47] However, FE models require a high mesh resolution around faults to accurately capture the onset of slip, resulting in computationally expensive models which prohibit any

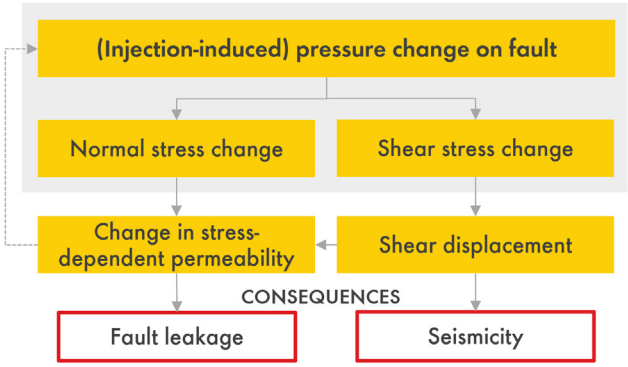

Figure 3. Changes in fault stress state (normal and shear stress) potentially impact the stress-dependent flow and reactivation potential of faults

robust sensitivity analysis. Mesh-free methods exist[48] but these methods still require a form of fault domain discretization that remains computationally expensive, whereas the objective of the Four Pillars workflow is to provide a fast screening of fault integrity. This screening approach requires an extensive uncertainty analysis considering a wide parameter space to capture the uncertainties associated with limitations in subsurface fault zone characterization, requiring a large number of model realizations.

Analytical CFS analyses methods such as the Fault Slip Potential (FSP) tool do accommodate extensive uncertainty quantifications.[49] FSP and similar analytical CFS methods provide an analysis of fault failure risk as a function of stress state, fault orientation, fault friction coefficient and pore pressure increase. These analytical methods have been used extensively for fault reactivation risk assessments.[50,51] Some of these methods account for the potential destabilizing effect of vertical fault offset, relative to reservoir thickness.[52–55] These latter studies indicate that for a population of faults within a CO_2 storage site the maximum pore pressure threshold required to ensure CO_2 containment with respect to frictional fault stability will depend on the most critically oriented faults with respect to the initial stress, with the largest fault throws exposed to the largest pore pressure increases. Fortunately, due to their size, these faults will be the most-readily recognizable. When considering suitable offset distances between existing faults and future injection well locations, these fault stability considerations mean larger throw faults will require larger offset distances than similarly oriented small throw faults. Not accounting for this effect could lead to an underestimation of the fault reactivation risk as the shear stress limit could otherwise be overestimated.[55]

To facilitate the mechanical risk ranking of faults, we develop a probabilistic analytical fault integrity analysis workflow for 3D fault geometries based on CFS analysis developed by Jansen et al.[56] to calculate the extent of failure along a fault based on the CFS criterion, using the fault throw to reservoir thickness ratio, Coulomb prestress and pore pressure change (Figure 4). The fault input geometries can be obtained from 3D seismic interpretations or structural framework models constrained by available subsurface data, with no need for upscaling or downsampling. The fault failure extent is calculated along densely spaced cross-section lines (pillars) oriented perpendicular to the local fault strike direction, using the local fault dip angle, reservoir thickness, and fault throw. To compare failure risks between different faults, the failure extent can be normalized by the length of the failed segment versus the vertical extent of the storage site or primary store seal. The workflow supports a range of data and models for input of stresses, pore pressure, fault geometries and mechanical fault and rock properties.

Uncertainties in the input data are included through a Monte Carlo analysis where for each stochastic realization, uncertainties drawn from the specified input distributions are added to the reference values per fault node for the fault failure calculation. For each reservoir-seal segment along a fault dip line, the local fault throw-reservoir thickness ratio and pore pressure change are used to calculate the fault failure risk. Perturbations throughout the storage site and life cycle in for example pore pressure can be included to calculate the change in fault failure risk in different parts of the model at different time steps. Dedicated visualizations including tornado charts, histograms, and cumulative distribution functions help to quantify and communicate risks and uncertainties in support of for example prioritization of additional

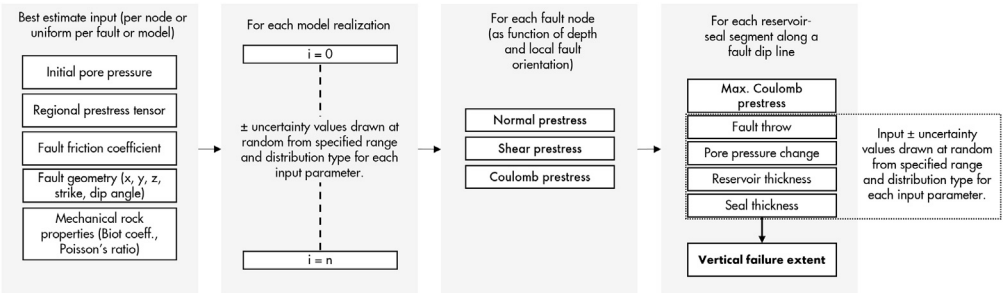

Figure 4. Flow diagram showing each calculation step in the probabilistic workflow between the inputs and the fault failure analysis

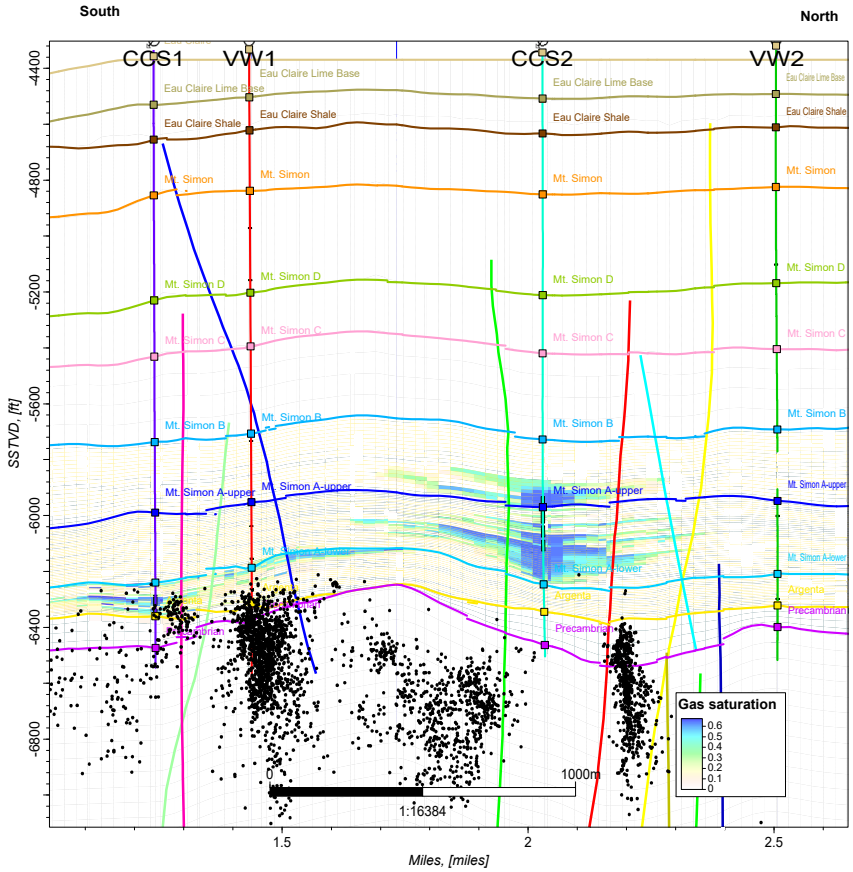

Figure 5. N-S cross-section (3x vertical excegeration) through the storage reservoir showing the simulated history-matched CO_2 saturation at the end of the two injection phases in January 2020 (Adapted from Zulaski and Lee[61])

The reservoir-basement interface is indicated by the purple line marked "Precambrian." The observed microseismic events during both injection phases are shown as black dots. The dipping lines represent mapped faults.

data acquisition or design of an MMV (Monitoring, Measuring, and Verification) program for site-specific monitoring of storage containment integrity. The probabilistic failure analysis is implemented into a dashboard through which the data can be loaded and failure extent models can be generated and visualized.

Application

Decatur carbon capture and sequestration project

Demonstrating the validity of fault failure models is challenged by the lack of direct observations of fault failure outside of a laboratory environment. In the subsurface, monitoring of (micro)seismic activity is commonly used to detect fault reactivation, but the absence of microseismic events does not confirm the absence of fault failure as failure could be expressed as aseismic slip. Aseismic slip can be measured using fiber-optic acoustic or strain sensing[41] but this technology requires a well that is within close proximity of an active fault. In this article, we will utilize a published dataset from the Decatur CCS project in Illinois, US[57] to illustrate the proposed workflow.

The Decatur CCS project injected 2.7 megaton of dense phase CO_2 into the Cambrian Mt. Simon Formation (Fm.) in two phases. During phase 1, 1.0 megaton of CO_2 was injected in well CCS1 at a depth of 2,140 m over a 3-year period from 2011 to 2014 into the deepest section of the reservoir, the Mt. Simon A Lower formation (Figure 5). In phase 2, 1.7 megaton of CO2 was injected via well CCS2 into the Mt. Simon An Upper and Mt. Simon B formations, during another 3-year period from 2017 to 2020. The horizontal distance between the two injectors is 1 km (Figure 6). Extensive seismic fault reactivation was observed during phase 1, compared to limited to no fault reactivation in phase 2, based on observations from microseismic monitoring.

This public dataset encompasses all relevant data for demonstrating the application of the probabilistic fault failure assessment, including the structural fault-horizon framework, history-matched pore pressure distribution and geomechanical stress and rock property distributions.[58] We apply the probabilistic fault failure assessment workflow and compare the results with numerical hydromechanical models developed by Luu et al.[35] for the same dataset. Fault reactivation is considered as a possible prior indicator of changes in fault leakage behavior. Forecasting seismic event activity is not within scope of this workflow as that requires dedicated probabilistic hazard and risk (PSHRA) workflows.[59,60]

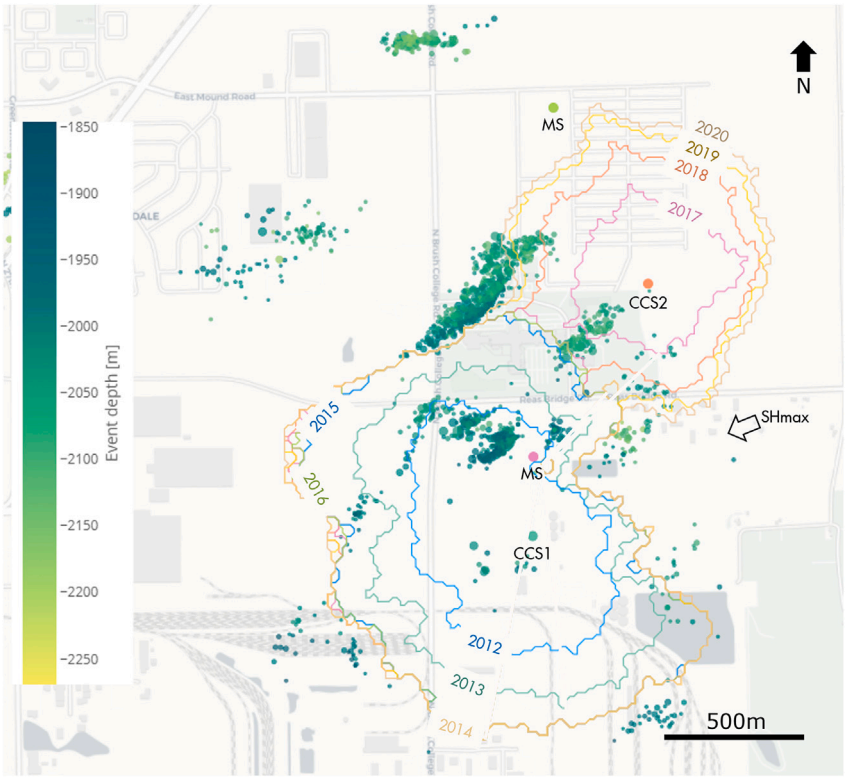

Figure 6. Map view of the two vertical injector wells CCS1 and CCS2, the two vertical downhole microseismic monitoring wells (marked MS), the distribution of microseismic events with magnitudes above the minimum magnitude of completeness detected between January 2011 and July 2018 (n = 1,885) and the colored contour lines indicating the temporal evolution of the CO_2 plume during the two injection phases, from 2012 to 2020

Model input parameters

As part of the Decatur project, the Illinois State Geological Survey (ISGS) has published 3D geological, reservoir engineering, and geomechanical models that have been developed using 3D seismic reflection data and well data (petrophysical logs and cores) obtained from the four wells drilled in the storage site and regional data.[58] The models were calibrated to reservoir surveillance data acquired during injection and these models form the basis for the fault stability analysis. The original input data and details of model development are published by the ISGS.[61] A detailed description of these models is out of scope but we discuss the elements that are used in the current study. The geological model provides the fault and horizon interpretations, as well as the distribution of reservoir thickness and throws along the faults. The Mt. Simon storage formations are approximately horizontal (<1° dip) with no folding and no significant lateral variation in reservoir rock properties.[62] In total, 28 faults have been modeled based on interpretations from 3D seismic reflection data (Figures 7A and 7B). The maximum measured vertical throw of these faults is 18 m (Figure 7C). The faults extend from the reservoir into the upper part of the Precambrian basement. Based on the observed microseismic activity, there are additional subseismic deformation features in the basement, which have been represented in a stochastic discrete fracture network model.[61] In the absence of direct observations of the exact location and geometries of these sub-seismic features, we focus on the 28 interpreted faults, acknowledging that these faults do not explain all observed seismic activity.

The reservoir pore pressure spatial distribution during injection is obtained from a history-matched reservoir flow model with pressures and saturations calibrated to available well data. Pore pressures are available at monthly time steps (Figure 8). The subsurface stress state has been characterized in detail by Luu et al.[35] based on data obtained from the monitoring and injection wells drilled during the project. The store is in a strike-slip faulting regime with the maximum horizontal stress oriented ENE-WSW (N068) based on a synthesis of borehole breakouts and regional data from the World Stress Map.[62,63] The minimum horizontal stress is derived from stress measurements obtained from hydraulic fracturing, overcoring and downhole borehole pressure data. The maximum horizontal stress gradient is not measured directly but calculated by assuming that the host rock is near critically stressed conditions. The overburden stress gradient is based on integrated density logs from the drilled wells in the storage site area.

The main evidence for fault reactivation comes from microseismic monitoring. Seismicity was monitored through two borehole arrays in the vicinity of the injector wells (Figure 6). Between 2011 and 2020, 5,350 events were detected with magnitudes ranging between −2.1 and 1.2, of which 1,885 are above the minimum magnitude of completeness $M_c = -0.7$ (Figure 9).[63,64] The spatiotemporal distribution of these events provides insights into the seismic failure behavior of faults. Most of the events were observed during the first phase of injection and

CellPress
OPEN ACCESS

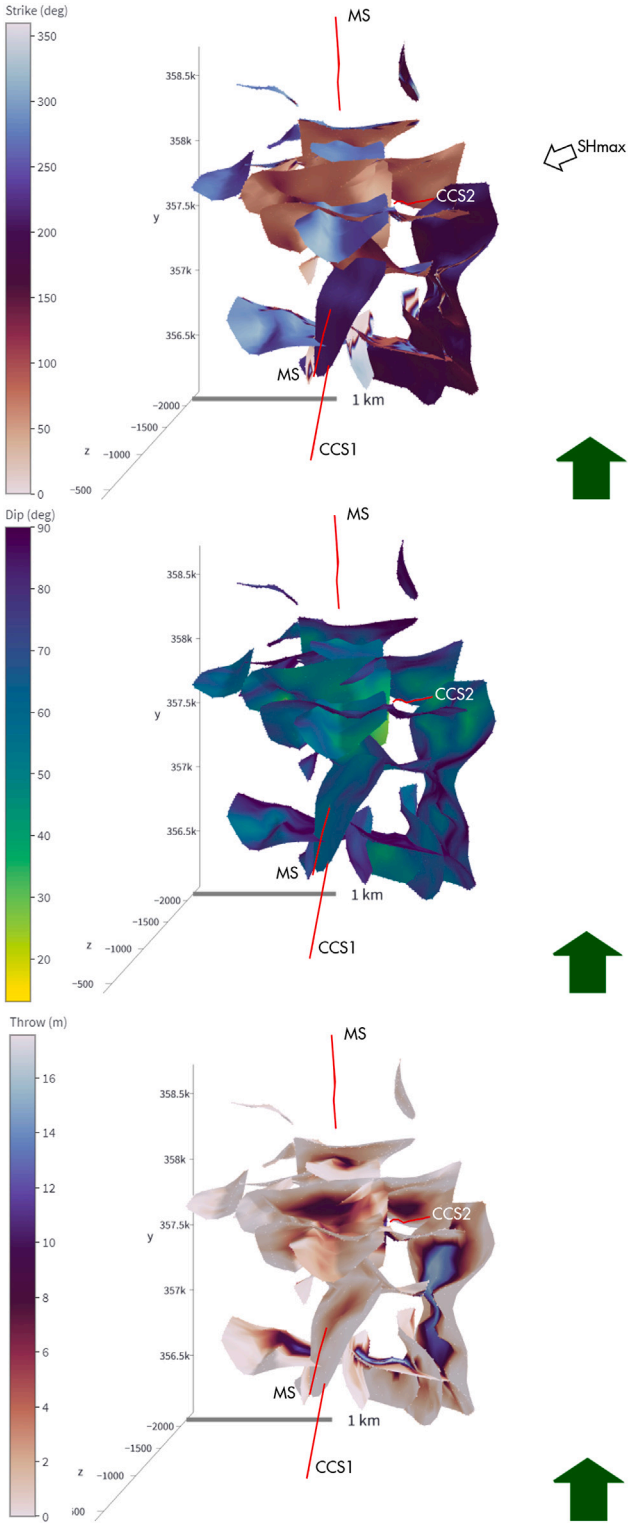

Figure 7. Top view (North is up) of the mapped reservoir faults colored by strike direction (top), dip angle (middle) and vertical throw (bottom)

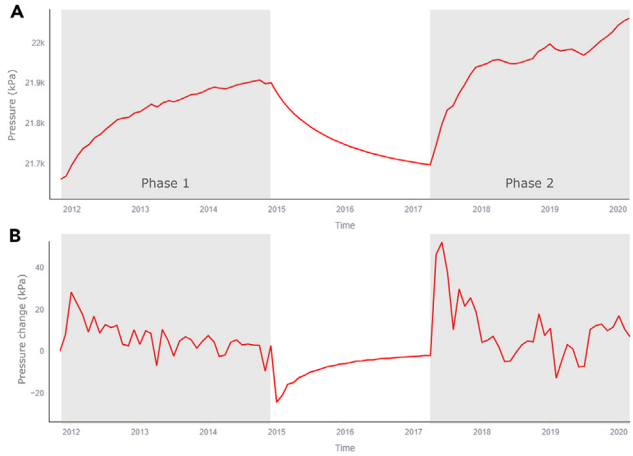

Figure 8. History-matched reservoir pore pressure distribution as a function of time during the two injectino phases

(A) Average reservoir pore pressure in kPa as a function of time calculated from the history-matched reservoir flow model.

(B) Rate of pressure change per monthly time step.

have been located in the basement (Figure 9), and have been attributed to basement fault reactivation during phase 1 of CO_2 injection, where the CO_2 was injected in the deepest section of the Mt. Simon formation, below a shale baffle. The injection-induced pore pressure increase could not be dissipated throughout the shallower part of the Mt. Simon reservoir rock, instead increasing the pressure in the basement faults in the absence of a bottom pressure seal between the Mt. Simon and basement formations.[64]

Clustering of microseismic events with a correlation of the cluster orientations with the regional maximum horizontal stress direction is observed, indicating that seismicity is not purely pressure-driven but at least in part influenced by pre-existing structural deformation.[64] The orientation of the long axis of clusters of microseismic events is predominantly NE-SW, sub-parallel to the regional orientation of the maximum horizontal stress. Although the mapped reservoir faults mostly continue into the basement, there is only a weak correlation between

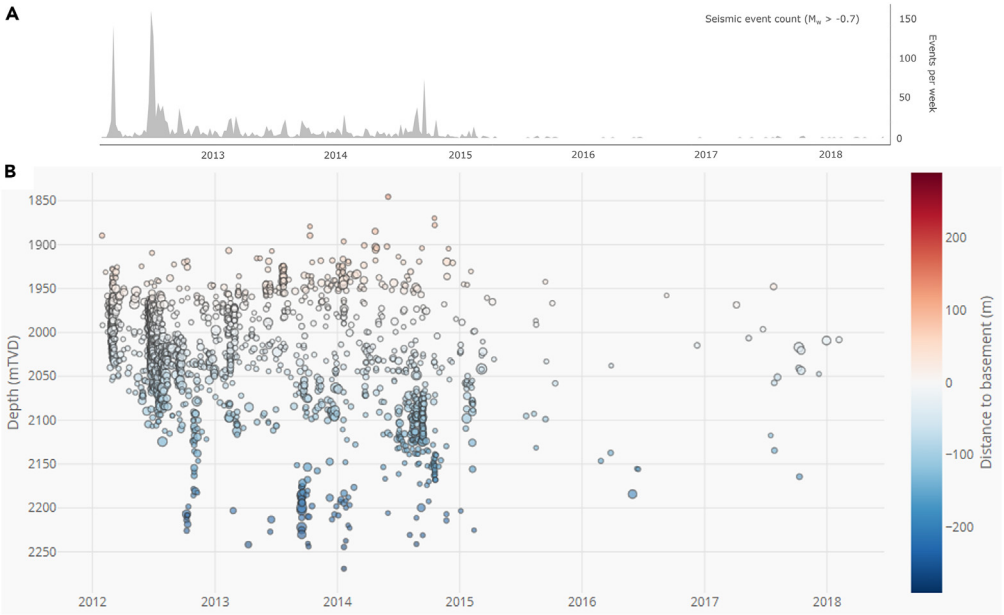

Figure 9. Recorded microseismic activity as a function of time

(A) Frequency of located microseismic events detected per week, including only events with magnitudes larger than the minimum magnitude of completeness (n = 1,185).

(B) Distribution of microseismic events with magnitudes above the minimum magnitude of completeness (n = 1,885) as a function of time. Symbol size scales with event magnitude and the symbol color represents the vertical distance from the event to the top of the basement. Positive values represent events above the basement and negative distances are events within the basement.

Table 1. Model base case and uncertainty parameters

Parameter	Base value	Sensitivity	Comments/source
Shmin gradient	16.4 kPa/m	±1 kPa/m	Using depth-dependent trends (reported values are averages) from Luu et al.[35]
Sv gradient	24 kPa/m	±0.3 kPa/m	Using depth-dependent trends (reported values are averages) from Luu et al.[35]
SHmax gradient	29 kPa/m	±1 kPa/m	Using depth-dependent trends (reported values are averages) from Luu et al.[35]
Virgin pore pressure	10.15 kPa/m	±0.2 kPa/m	Using depth-dependent trends (reported values are averages) from Luu et al.[35]
SHmax azimuth	N068°	±5°	Regional stress/frac data
Fault strike	Calculated per node	±20°	Interpreted surfaces
Fault dip angle	Calculated per node	±10°	Interpreted surfaces
Fault friction angle	35°	±10°	Based on assumption that faults are close to critically stressed prior to injection.
Fault throw	Calculated per node	±5 m	Exported from Petrel model, sensitivity based on standard deviation
Reservoir thickness	Calculated per node	±10 m	Calculated from Mt Simon A – Lower to Argenta, sensitivity based on thickness standard deviation
Seal thickness	10 m	±5 m	Mudstone baffle above Mount Simon A - lower

the spatial distribution of microseismic events and the mapped faults. The remaining microseismic events are likely associated with sub-seismic faults or fracture networks that cannot be interpreted from seismic in part because the interpretation is more challenging in the metamorphic rocks of the Precambrian basement.[64] The presence of fractures in the basement is confirmed from image logs,[64] but due to the uncertainties in the exact distribution and geometry of these features, only the interpreted faults are included in the fault stress models. The resulting models do not explain all observed seismicity due to the omission of sub-seismic features, but focus on capturing the seismicity around the mapped faults.

The *in-situ* pre-injection fault friction coefficient cannot be measured directly but is instead inferred from the regional stress state and the observed fault reactivation behavior. The pre-injection microseismic monitoring baseline shows no significant activity on the mapped faults, but faults are reactivated throughout the storage site following a relatively minor pressure increase during injection. These observations indicate that pre-injection, the faults are close to critically stressed. Using Equation 1 with the measured regional stress state and pore pressure, a fault friction angle of 35° best fits these observations. For this friction angle value, faults prior to injection are stable and become partly unstable during injection. However, a wide uncertainty range is considered for this parameter in the absence of direct measurements.

Using the fault stress assessment workflow with the abovementioned geometrical, rock mechanical, and stress state parameters we assess the likelihood of failure for both reservoir and basement segments of the mapped seismic faults during the two injection phases. The reference case model is based on the fault geometries as interpreted from seismic reflection data, combined with the history-matched pore pressure model and stress gradients and mechanical rock properties per formation as derived by Luu et al.[35] For the Monte Carlo uncertainty analysis, sensitivity ranges for all input parameters are defined based on scatter observed in the data (Table 1). For the stress gradients and orientation of the maximum horizontal stress component, uncertainty ranges are defined that include all observed stress measurements in the region.[62] A sensitivity range of ±10° is considered for the fault friction angle based on published measured values from a wide range of rock types. To account for subseismic faults with varying orientations, a scatter of ±20° is included for fault strike and ±10° for fault dip. The uncertainty range for fault throw is two standard deviations calculated from the observed throw distribution (±5 m). The same approach is used to define uncertainty ranges for reservoir (±10 m) and seal (±5 m) thicknesses.

During phase 1, pressure communication is allowed between the reservoir and the basement fault segments. The pressure distribution in the basement is not included in the history-matched flow model, instead the reservoir pore pressure distribution is vertically projected onto the basement faults. During phase 2, pore pressure changes are restricted to the reservoir interval only as injection is occurring above the shale baffle that forms a pressure barrier between the injection interval and the lowest part of the Mt. Simon formation and underlying basement (Figure 10).

RESULTS

Pre-injection stress state

The P50 Coulomb stress state prior to injection is negative and close to 0, governed by the choice for the average fault friction angle (Figure 11). The stress distribution for all fault nodes for all probabilistic realizations (n = 1,000) prior to injection considering the uncertainty ranges defined in Table 1 shows however a wider range (Figure 12). The long tail of negative stress values is related to subvertical NNW-SSE striking fault segments which strike normal to the regional maximum horizontal stress direction resulting in high normal and low shear stresses (Figure 13). Faults striking parallel to the regional maximum horizontal stress direction also have a low Coulomb stress whereas faults striking at a small angle (5–35°) relative to the maximum horizontal stress direction have the relative highest Coulomb stress, resulting from large shear stresses. In the strike-slip stress regime, the Coulomb stress increases with increasing fault dip angle. Although the average Coulomb stress

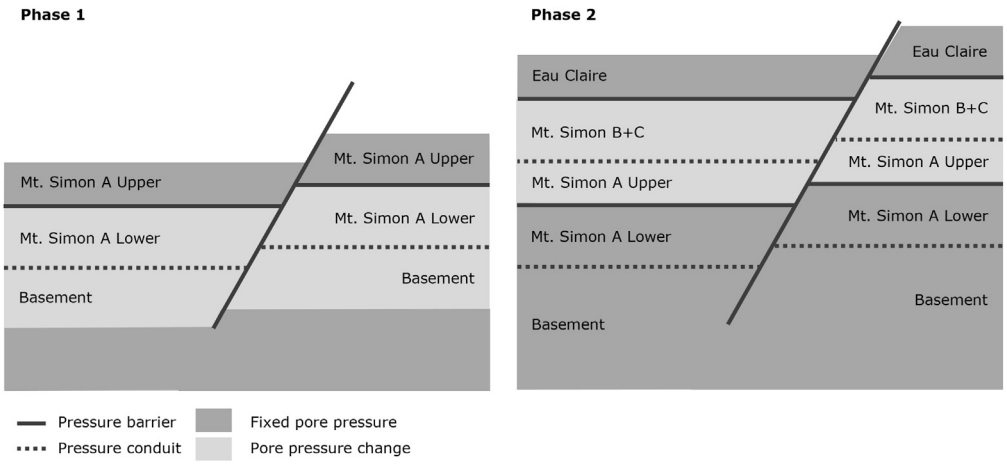

Figure 10. Schematic cross-sections of the two fault stress models considered during the two phases of CO_2 injection (not to scale)

per realization, averaged for all fault nodes, is negative in more than 90% of the realizations, the maximum Coulomb stress on individual nodes observed within each realization can be up to 10 MPa higher (Figure 14).

Injection-induced stress changes

The along-fault failure probability during the two injection phases is calculated given the same uncertainty ranges as used for the Coulomb prestress calculation (Table 1) and the spatially distributed history-matched pore pressure distribution at each monthly timestep. The absolute reservoir pressure prior to the start of both injection phases is approximately equal but the rate of change is higher at the onset of phase 2 compared to phase 1 (Figure 8B). The extent of the failed fault segments is calculated along each subvertical fault pillar and summed to obtain the failure extent for all faults for each realization (Figure 15). During both injection phases, the failure extent is highest at the onset of injection, corresponding to the largest increase in the rate of pore pressure change, and then decreases within the first six months. The initial increase in failure extent at the onset of injection is of comparable magnitude in both injection phases, but during continued injection the failure extent is higher in phase 1 compared to phase 2, when observing the 95% confidence interval of the simulations.

Within the explored uncertainty range for the model input parameters, there are scenarios that lead to failure and scenarios with no failure. Only during the first month of injection in both phases, non-zero failure is observed in 95% of the scenarios. The fault segments with the highest normalized failure extent are mostly striking sub-parallel to the regional maximum horizontal shortening direction (Figure 16). The orientation distribution of the failure extent is qualitatively comparable to the distribution of Coulomb prestress (compare Figure 13 with Figure 16). This direction is consistent with the NE-SW oriented clusters of microseismic events observed in the basement (Figure 17). Focusing on the first year of injection of phase 1, which corresponds with the period when the largest amount of seismicity was observed, the fault segments with the highest failure risk are those located close to the CCS1 injector well, where the pressure increase is highest, striking in an NE-SW direction. There is a partial overlap between these fault segments and the locations of the clusters of microseismic events. The events further away from faults are associated with subseismic fractures that were not included in the models due to lack of data.

DISCUSSION AND LIMITATIONS

Differences in normalized vertical failure extent between the two CO_2 injection phases are small but the modeled probability of failure during phase 1 is higher than during phase 2, even though the absolute and relative temporal pore pressure changes in phase 2 are larger compared to phase 1 (Figure 15). The higher probability of failure during phase 1 compared to phase 2 is not explained by the Coulomb prestress or the pore pressure change, but by a difference in the fault throw-reservoir thickness ratio between the two phases. In phase 1, pore pressure changes are limited to fault segments in the Mt. Simon A Lower formation and the upper part of the basement whereas in phase 2, pore pressure changes are confined to the entire Mt. Simon interval except Mt. Simon A Lower, which is significantly thicker. The resulting larger throw-thickness ratio in phase 1 relative to phase 2 contributes to a larger vertical failure extent under equal pore pressure changes as the pressure change threshold for failure decreases with increasing throw-thickness ratio.

Luu et al.[35] introduced vertical faults in the basement aligned with the spatial distribution of microseismic into their hydromechanical models of the Decatur site to model seismic fault reactivation during from the onset of the first injection phase into the first year of the second injection phase (November 2011 to April 2018). These models are based on the actual injection rates for wells CCS1 and CCS2, combined with a hydromechanical reservoir model to simulate spatiotemporal fluid flow and pressure changes in the reservoir and basement. The normalized fault failure extent calculation does not provide any assessment of seismicity, but in terms of failure probability changes between phase 1 and phase 2 the trend of a decrease in normalized vertical failure extent during phase 2 is consistent with the numerical model stress change results from Luu et al.[35]

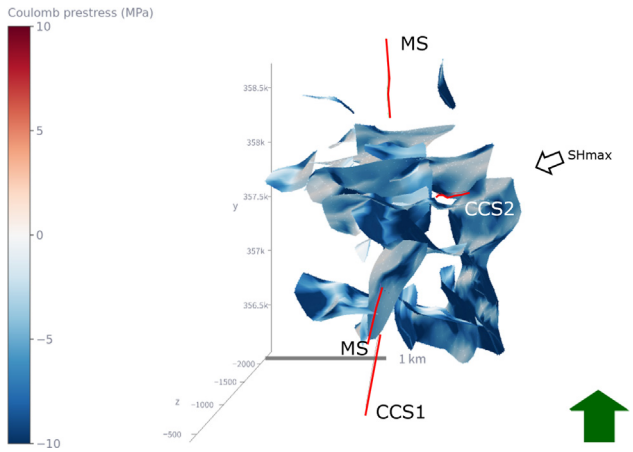

Figure 11. P50 distribution of Coulomb prestress per fault node

The mechanical fault failure analysis yields a relative ranking of differences in mechanical fault stability across faults in one or more prospective CO_2 storage sites, without the need for numerical 3-D finite element models. This screening is based on the failure likelihood of fault segments as a potential indicator of fault integrity risks but does not directly address the risk of microseismic events or leakage paths along faults. Leakage risks can be more comprehensively assessed by integrating this mechanical analysis with the geological, geometric and dynamic pillars for fault integrity. The Four Pillars for fault integrity were initially developed as a framework for identifying and mitigating fault integrity issues during drilling.[34] These same pillars can be used to assess and rank integrity risks across faults in geoenergy applications in the broader sense, including in CO_2 sequestration projects. A few key differences between the applications for drilling versus the updated framework for injection and storage include.

(1) Geometric de-risking: Instead of focusing on the intersection between wellbore and fault zone, the distance from injection points to faults should be considered.
(2) In case of wells drilled through faults, fault flow potential can be measured directly but fault-well intersections are typically avoided in CO_2 storage projects. Elements from the other three pillars can however be integrated to estimate the fault leakage potential, using core data and outcrop analogues.[15]
(3) The impact of the poroelastic effect and the dynamic flow injection behavior should be taken into consideration. We extend the original mechanical pillar to include a probabilistic Coulomb stress assessment as a function of for pore pressure variations and the fault geometry, including offset, which can introduce an additional destabilizing effect.[55]

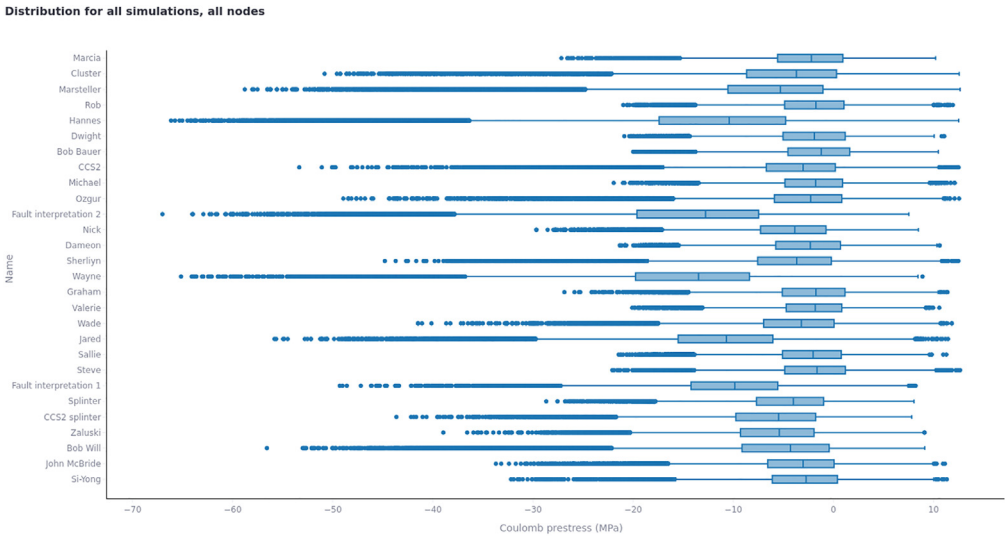

Figure 12. Full distribution of Coulomb prestress in a box-and-whisker plot for all 6,883 fault nodes, per fault, for all 1,000 realizations
The y axis lists the different faults.

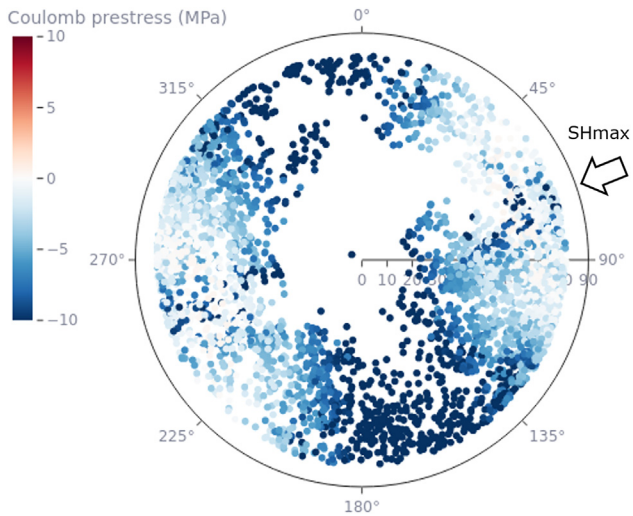

Figure 13. P50 Coulomb prestress distribution as a function of orientation for each individual fault node in the network (*n* = 6,883)

We recognize that geomechanical models may suggest faults can fail due to a prescribed stress condition,[65] but the static architecture of the fault damage zone and how fluid interact with the fault zone dynamically should not be overlooked during risk assessments.[66–69] A fault seal analysis without mechanical or dynamic evaluation can also mischaracterize the potential leakage threats from a fault. For instance, will a fault that acts as an across-fault flow barrier due to a high shear gauge ratio become prone to slippage because of pressure changes and create a new fault-parallel out-of-zone leak path? Different fluids may also affect fault seal potential in different ways, which has been studied to some extent for CO_2, indicating potentially different column height constraints for CO_2 compared to methane,[70,71] and may also play a role in storage of hydrogen.[9,72] The impact of subsurface operations on fault flow behavior is the ultimate question that the integrated Four Pillars framework aims to address.

Conclusions

The use of the subsurface for geoenergy applications, ranging from the exploration and development of hydrocarbon and geothermal sources to seasonal storage of hydrogen and permanent sequestration of CO_2 in depleted hydrocarbon fields or aquifers induces pore pressure changes which can lead to changes in the Coulomb stress along geological faults. Changes in the fault stress state could under certain conditions lead to mechanical fault failure, with possible consequences to the seismic susceptibility and leak potential of faults. Chan et al.[34] developed the Four Pillars workflow to identify leakage risks associated with drilling through faults. These Four Pillars capture the geological, geometric, mechanical and dynamic behavior of faults. We apply this workflow to assess fault integrity for CO_2 storage, extending the mechanical pillar to consider pore pressure changes in a storage reservoir with faults through a probabilistic analytical frictional fault stability framework for 3D fault geometries based on Coulomb Failure Stress. The resulting failure extent is used to assess the frictional fault stability throughout the storage site and storage life cycle. The workflow is fully probabilistic to allow for a robust uncertainty analysis of the impact of often poorly constrained reservoir and fault properties. The calculations can be applied directly on structural interpretations of faults with no need of time-intensive meshing or computationally expensive numerical models, as a first screening step for the assessment of integrity risks associated with the mechanical stability of faults in CCS projects.

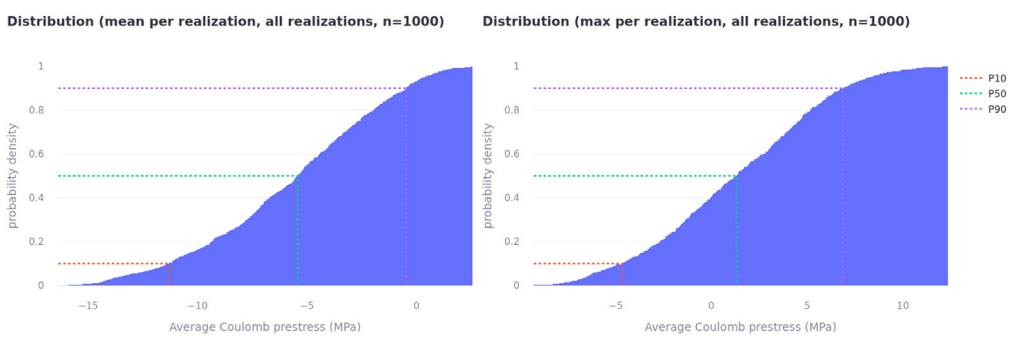

Figure 14. Average (left) and maximum Coulomb prestress based on all nodes in the fault network per realization (*n* = 1,000)

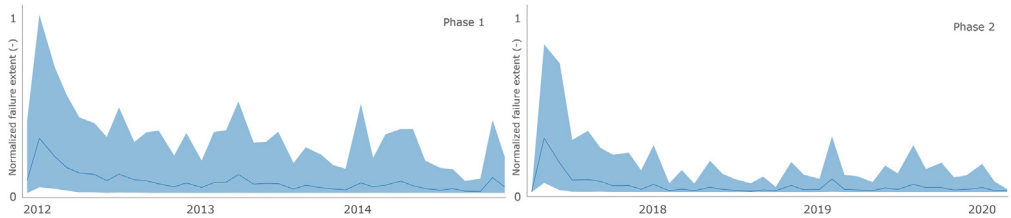

Figure 15. Along-fault vertical failure extent, normalized given the primary seal thickness, for each monthly pressure time step during phase 1 (left) and phase 2 (right) injection (n = 500)

The average failure extent is indicated by the blue curve, the light blue bands indicate the 95% confidence interval.

The mechanical integrity assessment is showcased using the Decatur Illinois CCS project. Model results show a high likelihood for fault failure during injection, with a higher failure probability during phase 1 relative to phase 2, even though injection pressures and rates were higher during phase 2. The higher fault throw to reservoir thickness ratio in the interval that is experiencing pressure changes during phase 1 relative to phase 2 is identified as the main reason for the difference in fault failure likelihood between the two injection phases. The difference in failure likelihood is consistent with hydromechanical numerical models developed using the same dataset,[35] although there is no direct measurement of the total amount of aseismic and seismic failure in the Decatur project to which the model results could be compared.

The extended mechanical analysis forms the third pillar of the Four Pillars developed by Chan et al.,[34] applied to CO_2 storage, providing an indication of fault integrity risks based on the fault stress state, but without providing a direct leakage assessment. The Fourth Pillar by Chan et al.[34] describes the dynamic properties based on data from wells intersecting faults. However, wells in subsurface storage projects are generally drilled away from faults, requiring the use of analogue data to quantify the fault leakage risk. The dynamic fault characterization workflow based on lab and outcrop data developed by Snippe et al.[15] can be used in combination with the mechanical workflow in this study to form an updated Four Pillars approach toward derisking faults in CO_2 storage projects.

STAR★METHODS

Detailed methods are provided in the online version of this paper and include the following:

- KEY RESOURCES TABLE
- RESOURCE AVAILABILITY
  - Lead contact

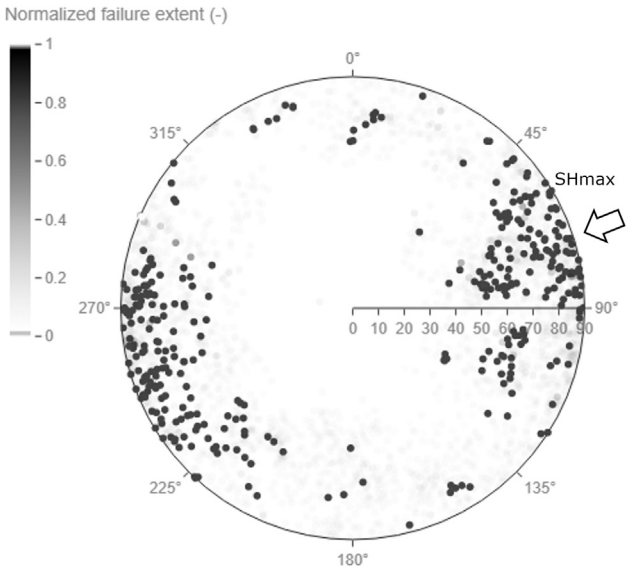

Figure 16. Stereoplot with the orientation of fault nodes (strike angle and dip angle) colored by the normalized vertical fault failure extent, where 1 indicates the extent of the failure alung the fault is equal to the thickness of the primary seal, and 0 indicates no failure along the fault

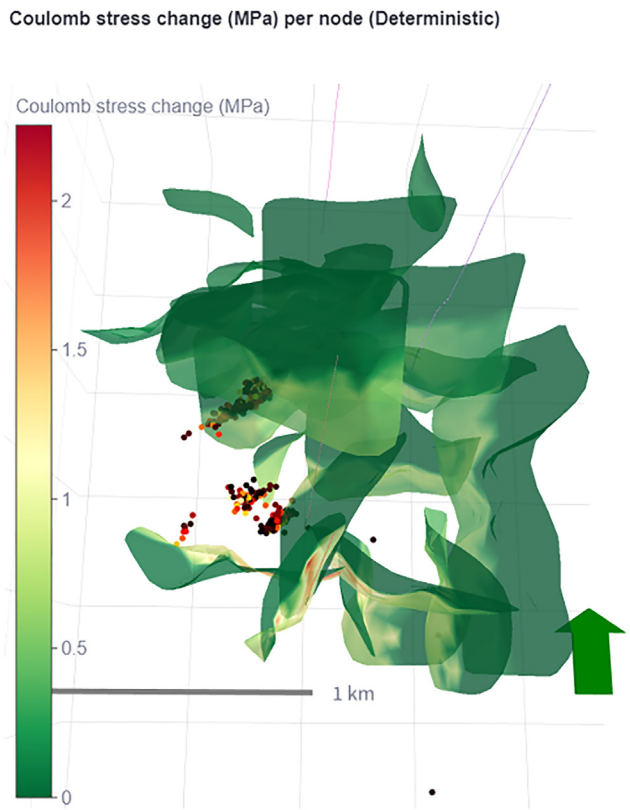

Figure 17. 3-D view of the P50 model Coulomb stress change results after one year of injection during phase 1 compared to the distribution of microseismic events observed during the same period (points colored by magnitude, darker colors indicating smaller magnitude events)

- Materials availability
- Data and code availability
- METHOD DETAILS
  - Coulomb failure stress analysis
- QUANTIFICATION AND STATISTICAL ANALYSIS

ACKNOWLEDGMENTS

The authors would like to acknowledge Shell Global Solutions International B.V. for funding and permitting publication of this work, as well as numerous (ex-)Shell colleagues for fruitful discussions and new insights. The dataset used in this study is available from the Illinois State Geological Survey (ISGS): Illinois Basin - Decatur Project (IBDP) CO_2 Injection Monitoring Data, April 30, 2021 - Midwest Geological Sequestration Consortium (MGSC) phase III Data Sets - DOE Cooperative Agreement No. DE-FC26-05NT42588 (https://doi.org/10.11582/2022.00017).

AUTHOR CONTRIBUTIONS

Conceptualization, K.B. and A.W.C; methodology, K.B. and A.W.C.; investigation, K.B.; writing – original draft, K.B. and A.W.C.; writing – review and editing, K.B. and A.W.C.

DECLARATION OF INTERESTS

K.B. is affiliated with Shell Global Solutions International B.V., A.W.C. is affiliated with Shell Global Solutions UK. Both authors declare they have no other affiliations.

Received: December 18, 2023
Revised: April 2, 2024
Accepted: May 8, 2024
Published: May 10, 2024

CellPress
OPEN ACCESS

REFERENCES

1. Davis, S.J., Lewis, N.S., Shaner, M., Aggarwal, S., Arent, D., Azevedo, I.L., Benson, S.M., Bradley, T., Brouwer, J., Chiang, Y.M., et al. (2018). Net-zero emissions energy systems. Science *360*, eaas9793. https://doi.org/10.1126/science.aas9793.
2. Hepple, R.P., and Benson, S.M. (2005). Geologic storage of carbon dioxide as a climate change mitigation strategy: Performance requirements and the implications of surface seepage. Environ. Geol. *47*, 576–585. https://doi.org/10.1007/s00254-004-1181-2.
3. Duong, C., Bower, C., Hume, K., Rock, L., and Tessarolo, S. (2019). Quest carbon capture and storage offset project: Findings and learnings from 1st reporting period. Int. J. Greenh. Gas Control *89*, 65–75. https://doi.org/10.1016/j.ijggc.2019.06.001.
4. Furre, A.K., Meneguolo, R., Ringrose, P., and Kassold, S. (2019). Building confidence in CCS: From sleipner to the northern Lights project. First Break *37*, 81–87. https://doi.org/10.3997/1365-2397.n0038.
5. Ringrose, P.S. (2018). The CCS hub in Norway: Some insights from 22 years of saline aquifer storage. Energy Proc. *146*, 166–172. https://doi.org/10.1016/j.egypro.2018.07.021.
6. Ringrose, P. (2020). How to Store CO2 Underground: Insights from Early-Mover CCS Projects (Springer International Publishing). https://doi.org/10.1007/978-3-030-33113-9.
7. Ringrose, P.S., and Meckel, T.A. (2019). Maturing global CO_2 storage resources on offshore continental margins to achieve 2DS emissions reductions. Sci. Rep. *9*, 17944. https://doi.org/10.1038/s41598-019-54363-z.
8. Rock, L., O'Brien, S., Tessarolo, S., Duer, J., Bacci, V.O., Hirst, B., Randell, D., Helmy, M., Blackmore, J., Duong, C., et al. (2017). The Quest CCS Project: 1st Year Review Post Start of Injection. Energy Proc. *114*, 5320–5328. https://doi.org/10.1016/j.egypro.2017.03.1654.
9. Heinemann, N., Alcalde, J., Miocic, J.M., Hangx, S.J.T., Kallmeyer, J., Ostertag-Henning, C., Hassanpouryouzband, A., Thaysen, E.M., Strobel, G.J., Schmidt-Hattenberger, C., et al. (2021). Enabling large-scale hydrogen storage in porous media-the scientific challenges. Energy Environ. Sci. *14*, 853–864. https://doi.org/10.1039/d0ee03536j.
10. Chen, M., Buscheck, T.A., Wagoner, J.L., Sun, Y., White, J.A., Chiaramonte, L., and Aines, R.D. (2013). Analysis of fault leakage from Leroy underground natural gas storage facility, Wyoming, USA. Hydrogeol. J. *21*, 1429–1445. https://doi.org/10.1007/s10040-013-1020-1.
11. Foschi, M., and Van Rensbergen, P. (2022). Topseal integrity assessment using seal properties and leakage phenomena. Mar. Petrol. Geol. *139*, 105573. https://doi.org/10.1016/j.marpetgeo.2022.105573.
12. Dockrill, B. (2005). Understanding Leakage from a Fault-Sealed CO2 Reservoir in East-Central Utah: A Natural Analogue Applicable to CO2 Storage.
13. Kampman, N., Busch, A., Bertier, P., Snippe, J., Hangx, S., Pipich, V., Di, Z., Rother, G., Harrington, J.F., Evans, J.P., et al. (2016). Observational evidence confirms modelling of the long-term integrity of CO2-reservoir caprocks. Nat. Commun. *7*, 12268. https://doi.org/10.1038/ncomms12268.
14. Miocic, J.M., Gilfillan, S.M.V., Frank, N., Schroeder-Ritzrau, A., Burnside, N.M., and Haszeldine, R.S. (2019). 420,000 Year Assessment of Fault Leakage Rates Shows Geological Carbon Storage Is Secure. Sci. Rep. *9*, 769. https://doi.org/10.1038/s41598-018-36974-0.
15. Snippe, J., Kampman, N., Bisdom, K., Tambach, T., March, R., Maier, C., Phillips, T., Inskip, N.F., Doster, F., and Busch, A. (2022). Modelling of long-term along-fault flow of CO2 from a natural reservoir. Int. J. Greenh. Gas Control *118*, 103666. https://doi.org/10.1016/j.ijggc.2022.103666.
16. Bense, V.F., Gleeson, T., Loveless, S.E., Bour, O., and Scibek, J. (2013). Fault zone hydrogeology. Earth Sci. Rev. *127*, 171–192. https://doi.org/10.1016/j.earscirev.2013.09.008.
17. Bense, V.F., and Person, M.A. (2006). Faults as conduit-barrier systems to fluid flow in siliciclastic sedimentary aquifers. Water Resour. Res. *42*, 1–18. https://doi.org/10.1029/2005WR004480.
18. Freeman, B., Yielding, G., Needham, D.T., and Badley, M.E. (1998). Fault seal prediction: the gouge ratio method. Geol. Soc. Spec. Publ. *127*, 19–25.
19. Yielding, G., Freeman, B., and Needham, D.T. (1997). Quantitative fault seal prediction. Am. Assoc. Petrol. Geol. Bull. *81*, 897–917. https://doi.org/10.1306/522B498D-1727-11D7-8645000102C1865D.
20. Yielding, G., Bretan, P., and Freeman, B. (2010). Fault seal calibration: a brief review. Geol. Soc. Lond. Spec. Publ. *347*, 243–255. https://doi.org/10.1144/SP347.14.
21. Solum, J.G., and Huisman, B.A.H. (2017). Toward the creation of models to predict static and dynamic fault-seal potential in carbonates. Petrol. Geosci. *23*, 70–91. https://doi.org/10.1144/petgeo2016-044.
22. Cappa, F., and Rutqvist, J. (2011). Modeling of coupled deformation and permeability evolution during fault reactivation induced by deep underground injection of CO2. Int. J. Greenh. Gas Control *5*, 336–346. https://doi.org/10.1016/j.ijggc.2010.08.005.
23. Wibberley, C.A.J., Yielding, G., Di Toro, G., Toro, G.D.I., Wibberley, C.A.J., Yielding, G., Toro, G.D.I., Einstein, A., House, N.B., Lane, N.B., et al. (2008). Recent advances in the understanding of fault zone internal structure: a review. Geol. Soc. Lond. Spec. Publ. *299*, 5–33. https://doi.org/10.1144/SP299.2.
24. Feitz, A.J., Radke, B., Radke, B.M., and Urosevic, M. (2018). The CO2CRC Otway shallow CO2 controlled release experiment : Geological model and CO2 migration simulations The CO2CRC Otway shallow CO 2 controlled release experiment : Geological model and CO 2 migration simulations. In 14th International Conference on Greenhouse Gas Control Technologies. GHGT-14.
25. Cerasi, P., Stroisz, A., Sønstebø, E., Stanchits, S., Oye, V., and Bauer, R. (2018). Experimental investigation of injection pressure effects on fault reactivation for CO2storage. Int. J. Greenh. Gas Control *78*, 218–227. https://doi.org/10.1016/j.ijggc.2018.08.011.
26. Dockrill, B., and Shipton, Z.K. (2010). Structural controls on leakage from a natural CO2geologic storage site: Central Utah, U.S.A. J. Struct. Geol. *32*, 1768–1782. https://doi.org/10.1016/j.jsg.2010.01.007.
27. Jung, N.H., Han, W.S., Watson, Z.T., Graham, J.P., and Kim, K.Y. (2014). Fault-controlled CO2leakage from natural reservoirs in the Colorado Plateau, East-Central Utah. Earth Planet. Sci. Lett. *403*, 358–367. https://doi.org/10.1016/j.epsl.2014.07.012.
28. Song, Y., Jun, S., Na, Y., Kim, K., Jang, Y., and Wang, J. (2023). Geomechanical challenges during geological CO2 storage: A review. Preprint at (Elsevier B.V.). https://doi.org/10.1016/j.cej.2022.140968.
29. Shotton, P., Vidal-Gilbert, S., Thibeau, S., Agenet, N., Lesueur, A., Manhes, C., and Ninet, C. (2022). Aramis CO2 storage Case Study - A Geomechanical Assessment of Containment (November 20, 2022). Proceedings of the 16th Greenhouse Gas Control Technologies Conference (GHGT-16), 23–24. https://doi.org/10.2139/ssrn.4282320.
30. Tao, Q., Alexander, D., and Bryant, S.L. (2013). Modeling potential CO2 leakage rate along a fault in Mahogany Field. J. Pet. Sci. Eng. *111*, 15–24. https://doi.org/10.1016/j.petrol.2013.10.003.
31. Zheng, X., and Espinoza, D.N. (2022). Stochastic quantification of CO2 fault sealing capacity in sand-shale sequences. Mar. Petrol. Geol. *146*, 105961. https://doi.org/10.1016/J.MARPETGEO.2022.105961.
32. Miocic, J.M., Johnson, G., and Gilfillan, S.M.V. (2020). Stress field orientation controls on fault leakage at a natural CO2 reservoir. Solid Earth *11*, 1361–1374. https://doi.org/10.5194/se-11-1361-2020.
33. Castelletto, N., Teatini, P., Gambolati, G., Bossie-Codreanu, D., Vincké, O., Daniel, J.M., Battistelli, A., Marcolini, M., Donda, F., and Volpi, V. (2013). Multiphysics modeling of CO2 sequestration in a faulted saline formation in Italy. Adv. Water Resour. *62*, 570–587. https://doi.org/10.1016/j.advwatres.2013.04.006.
34. Chan, A.W., Brem, A.G., Abd Rahim, M.H., Numpang, A., and Chong, S. (2022). The Four Pillars for De-Risking Fluid Loss Potential Along Fault Damage Zone: A Framework for Well Designs and Drilling Operations. In 56th U.S. Rock Mechanics/Geomechanics Symposium, Santa Fe, New Mexico, USA (ARMA). https://doi.org/10.56952/ARMA-2022-0197.
35. Luu, K., Schoenball, M., Oldenburg, C.M., and Rutqvist, J. (2022). Coupled Hydromechanical Modeling of Induced Seismicity From CO2 Injection in the Illinois Basin. J. Geophys. Res. Solid Earth *127*, e2021JB023496. https://doi.org/10.1029/2021JB023496.
36. Chan, A.W., Murray, D., De Gennaro, S., and O'Reilly, G. (2023). Can Lost Circulation Materials (LCM) Cure Losses Across Fault Damage Zone? In ARMA US Rock Mechanics/Geomechanics Symposium. https://doi.org/10.56952/arma-2023-0478.
37. Michie, E.A.H., Kaminskaite, I., Cooke, A.P., Fisher, Q.J., Yielding, G., and Tobiss, S.D. (2021). Along-strike permeability variation in carbonate-hosted fault zones. J. Struct. Geol. *142*, 104236. https://doi.org/10.1016/j.jsg.2020.104236.
38. Phillips, T., Bultreys, T., Bisdom, K., Kampman, N., Van Offenwert, S., Mascini, A., Cnudde, V., and Busch, A. (2021). A Systematic Investigation into the Control of Roughness on the Flow Properties of 3D-

Printed Fractures. Water Resour. Res. *57*, 1–23. https://doi.org/10.1029/2020wr028671.
39. Cappa, F., Guglielmi, Y., Nussbaum, C., De Barros, L., and Birkholzer, J. (2022). Fluid migration in low-permeability faults driven by decoupling of fault slip and opening. Nat. Geosci. *15*, 747–751. https://doi.org/10.1038/s41561-022-00993-4.
40. Guglielmi, Y., Birkholzer, J., Rutqvist, J., Jeanne, P., and Nussbaum, C. (2017). Can Fault Leakage Occur Before or Without Reactivation? Results from an in Situ Fault Reactivation Experiment at Mont Terri. Energy Proc. *114*, 3167–3174. https://doi.org/10.1016/j.egypro.2017.03.1445.
41. Guglielmi, Y., Nussbaum, C., Jeanne, P., Rutqvist, J., Cappa, F., and Birkholzer, J. (2020). Complexity of Fault Rupture and Fluid Leakage in Shale: Insights From a Controlled Fault Activation Experiment. J. Geophys. Res. Solid Earth *125*, 1–19. https://doi.org/10.1029/2019JB017781.
42. Jeanne, P., Guglielmi, Y., Rutqvist, J., Nussbaum, C., and Birkholzer, J. (2018). Permeability Variations Associated With Fault Reactivation in a Claystone Formation Investigated by Field Experiments and Numerical Simulations. J. Geophys. Res. Solid Earth *123*, 1694–1710. https://doi.org/10.1002/2017JB015149.
43. Wiprut, D., and Zoback, M.D. (2000). Fault reactivation and fluid flow along a previously dormant normal fault in the Northern North Sea. Geology *28*, 595–598. https://doi.org/10.1130/0091-7613(2000)28<595:FRAFFA>2.0.CO;2.
44. Hunfeld, L.B., Niemeijer, A.R., and Spiers, C.J. (2017). Frictional Properties of Simulated Fault Gouges from the Seismogenic Groningen Gas Field Under In Situ P - T -Chemical Conditions. J. Geophys. Res. Solid Earth *122*, 8969–8989. https://doi.org/10.1002/2017JB014876.
45. Brem, A.G., Abd Rahim, M.H., Zhang, T., and Chan, A.W. (2019). How strong is your fault? In 53rd U.S. Rock Mechanics/Geomechanics Symposium.
46. Rutqvist, J., Birkholzer, J., Cappa, F., and Tsang, C.F. (2007). Estimating maximum sustainable injection pressure during geological sequestration of CO2 using coupled fluid flow and geomechanical fault-slip analysis. Energy Convers. Manag. *48*, 1798–1807. https://doi.org/10.1016/j.enconman.2007.01.021.
47. Rutqvist, J., Rinaldi, A.P., Cappa, F., Jeanne, P., Mazzoldi, A., Urpi, L., Guglielmi, Y., and Vilarrasa, V. (2016). Fault activation and induced seismicity in geological carbon storage – Lessons learned from recent modeling studies. J. Rock Mech. Geotech. Eng. *8*, 789–804. https://doi.org/10.1016/j.jrmge.2016.09.001.
48. Van Wees, J.D., Pluymaekers, M., Osinga, S., Fokker, P., Van Thienen-Visser, K., Orlic, B., Wassing, B., Hegen, D., and Candela, T. (2019). 3-D mechanical analysis of complex reservoirs: A novel mesh-free approach. Geophys. J. Int. *219*, 1118–1130. https://doi.org/10.1093/gji/ggz352.
49. Walsh, F.R., and Zoback, M.D. (2016). Probabilistic assessment of potential fault slip related to injection-induced earthquakes: Application to north central Oklahoma, USA. Geology *44*, 991–994. https://doi.org/10.1130/G38275.1.
50. Dvory, N.Z., and Zoback, M.D. (2021). Assessing Fault Slip Potential in a Continuously Varying Stress Field – Application in the Delaware Basin. Preprint.
51. Hennings, P.H., Lund Snee, J., Osmond, J.L., DeShon, H.R., Dommisse, R., Horne, E., Lemons, C., and Zoback, M.D. (2019). Injection-Induced Seismicity and Fault-Slip Potential in the Fort Worth Basin, Texas. Bull. Seismol. Soc. Am. *109*, 1615–1634. https://doi.org/10.1785/0120190017.
52. Bourne, S.J., and Oates, S.J. (2017). Development of statistical geomechanical models for forecasting seismicity induced by gas production from the Groningen field. Neth. J. Geosci. *96*, s175–s182. https://doi.org/10.1017/njg.2017.35.
53. Buijze, L., van den Bogert, P.A.J., Wassing, B.B.T., and Orlic, B. (2019). Nucleation and Arrest of Dynamic Rupture Induced by Reservoir Depletion. J. Geophys. Res. Solid Earth *124*, 3620–3645. https://doi.org/10.1029/2018JB016941.
54. Buijze, L., van den Bogert, P.A., Wassing, B.B., Orlic, B., and ten Veen, J. (2017). Fault reactivation mechanisms and dynamic rupture modelling of depletion-induced seismic events in a Rotliegend gas reservoir. Neth. J. Geosci. *96*, s131–s148. https://doi.org/10.1017/njg.2017.27.
55. van den Bogert, P.A.J., and van Eijs, R.M.H.E. (2020). Why Mohr-circle analyses may underestimate the risk of fault reactivation in depleting reservoirs. Int. J. Rock Mech. Min. Sci. *136*, 104502. https://doi.org/10.1016/j.ijrmms.2020.104502.
56. Jansen, J.D., Singhal, P., and Vossepoel, F.C. (2019). Insights From Closed-Form Expressions for Injection- and Production-Induced Stresses in Displaced Faults. J. Geophys. Res. Solid Earth *124*, 7193–7212. https://doi.org/10.1029/2019JB017932.
57. Bauer, R.A., Will, R., E. Greenberg, S., and Whittaker, S.G. (2019). Illinois Basin–Decatur Project. In Geophysics and Geosequestration (Cambridge University Press), pp. 339–370. https://doi.org/10.1017/9781316480724.020.
58. Illinois State Geological Survey, US Department of Energy, Archer Daniels Midland Company, Schlumberger, and Trimeric Corporation (2022). Illinois Basin - Decatur Project Dataset. https://doi.org/10.11582/2022.00017.
59. Bourne, S.J., and Oates, S.J. (2017). Extreme Threshold Failures Within a Heterogeneous Elastic Thin Sheet and the Spatial-Temporal Development of Induced Seismicity Within the Groningen Gas Field. J. Geophys. Res. Solid Earth *122*, 299–320. https://doi.org/10.1002/2017JB014356.
60. Smith, J.D., Heimison, E.D., Avouac, J.-P., and Bourne, S. (2021). Stress-based forecasting of induced seismicity with instantaneous earthquake failure functions: Applications to the Groningen Gas Reservoir. Earth Planet. Sci. Lett. *594*, 117697. https://doi.org/10.1016/j.epsl.2022.117697.
61. Zaluski, W., and Lee, S. (2020). IBDP Final Static Geological Model Development and Dynamic Modelling.
62. Bauer, R.A., Carney, M., and Finley, R.J. (2016). Overview of microseismic response to CO2 injection into the Mt. Simon saline reservoir at the Illinois Basin-Decatur Project. Int. J. Greenh. Gas Control *54*, 378–388. https://doi.org/10.1016/J.IJGGC.2015.12.015.
63. Williams-Stroud, S., Bauer, R., Leetaru, H., Oye, V., Stanek, F., Greenberg, S., and Langet, N. (2020). Analysis of microseismicity and reactivated fault size to assess the potential for felt events by co2 injection in the illinois basin. Bull. Seismol. Soc. Am. *110*, 2188–2204. https://doi.org/10.1785/0120200112.
64. Goertz-Allmann, B.P., Gibbons, S.J., Oye, V., Bauer, R., and Will, R. (2017). Characterization of induced seismicity patterns derived from internal structure in event clusters. J. Geophys. Res. Solid Earth *122*, 3875–3894. https://doi.org/10.1002/2016JB013731.
65. Barton, C.A., Zoback, M.D., and Moos, D. (1995). Fluid flow along potentially active faults in crystalline rock. Geol. *23*, 683. https://doi.org/10.1130/0091-7613(1995)023<0683:FFAPAF>2.3.CO;2.
66. Jolley, S.J., Barr, D., Walsh, J.J., and Knipe, R.J. (2007). Structurally Complex Reservoirs G. S. Of London.
67. Knipe, R.J., Jones, G., and Fisher, Q.J. (1998). Faulting, fault sealing and fluid flow in hydrocarbon reservoirs: an introduction. Geol. Soc. Lond. Spec. Publ. *147*. vii–xxi. https://doi.org/10.1144/GSL.SP.1998.147.01.01.
68. Saló-Salgado, L., Davis, J.S., and Juanes, R. (2022). Fault permeability from stochastic modeling of clay smears. Geology *51*, 91–95. https://doi.org/10.1130/G50739.1.
69. Vrolijk, P.J., Urai, J.L., and Kettermann, M. (2016). Clay smear: Review of mechanisms and applications. J. Struct. Geol. *86*, 95–152. https://doi.org/10.1016/J.JSG.2015.09.006.
70. Miocic, J.M., Johnson, G., and Bond, C.E. (2019). Uncertainty in fault seal parameters: implications for CO2 column height retention and storage capacity in geological CO2 storage projects. Solid Earth *10*, 951–967. https://doi.org/10.5194/se-10-951-2019.
71. Naylor, M., Wilkinson, M., and Haszeldine, R.S. (2011). Calculation of CO2 column heights in depleted gas fields from known pre-production gas column heights. Mar. Petrol. Geol. *28*, 1083–1093. https://doi.org/10.1016/j.marpetgeo.2010.10.005.
72. Al-Mukainah, H., Al-Yaseri, A., Yekeen, N., Hamad, J.A., and Mahmoud, M. (2022). Wettability of shale–brine–H2 system and H2-brine interfacial tension for assessment of the sealing capacities of shale formations during underground hydrogen storage. Energy Rep. *8*, 8830–8843. https://doi.org/10.1016/j.egyr.2022.07.004.

CellPress
OPEN ACCESS

STAR★METHODS

KEY RESOURCES TABLE

REAGENT or RESOURCE	SOURCE	IDENTIFIER
Deposited data		
Illinois Basin - Decatur Project Dataset	CO2 DataShare - https://co2datashare.org/dataset/illinois-basin-decatur-project-dataset	https://doi.org/10.11582/2022.00017
Software and algorithms		
Insights From Closed-Form Expressions for Injection- and Production-Induced Stresses in Displaced Faults (JGR Solid Earth Research Article)	Matlab code - https://doi.org/10.4121/uuid:d8ca79ae-17fb-4c60-b86b-08c495b2722f	https://doi.org/10.4121/uuid:d8ca79ae-17fb-4c60-b86b-08c495b2722f

RESOURCE AVAILABILITY

Lead contact

Further information and requests for resources should be directed to and will be fulfilled by the lead contact, Kevin Bisdom (kevin.bisdom@shell.com).

Materials availability

This study did not generate any new materials.

Data and code availability

- All data reported in this paper will be shared by the lead contact upon request.
- This paper does not report original code.
- Any additional information required to reanalyze the data reported in this paper is available from the lead contact upon request.

METHOD DETAILS

Coulomb failure stress analysis

The main method used in this manuscript is the semianalytical Coulomb Failure Stress analysis applied to the digital dataset of the Illinois Basin – Decatur Project. The method is applied to the full deterministic dataset.

QUANTIFICATION AND STATISTICAL ANALYSIS

Statistical analysis was performed using standard Monte Carlo analysis. The sample size for all datasets is included in the figures and figure captions. The random seeds used for the probabilistic analyses are stored as part of the results datasets.